International Journal of Biological Macromolecules 130 (2019) 333–341

Contents lists available at ScienceDirect

International Journal of Biological Macromolecules

journal homepage: http://www.elsevier.com/locate/ijbiomac

Uricase grafted nanoconducting matrix based electrochemical biosensor for ultrafast uric acid detection in human serum samples

Shilpi Verma [a,b], Jyoti Choudhary [a,b], Krishna P. Singh [c], Pranjal Chandra [d], Surinder P. Singh [a,b,*]

[a] Academy of Scientific and Innovative Research (AcSIR), CSIR - National Physical Laboratory (Campus), New Delhi 110012, India
[b] CSIR - National Physical Laboratory, New Delhi 110012, India
[c] CCS Haryana Agricultural University, Hisar 125004, Haryana, India
[d] Laboratory of Bio-Physio Sensors and Nanobioengineering, Department of Biosciences and Bioengineering, Indian Institute of Technology Guwahati, Guwahati 781039, Assam, India

ARTICLE INFO

Article history:
Received 4 December 2018
Received in revised form 8 February 2019
Accepted 20 February 2019
Available online 21 February 2019

Keywords:
Uric acid
Uricase
Gold nanoparticles
Reduced graphene oxide
Electrochemical biosensor

ABSTRACT

Gold nanoparticles decorated graphene oxide (Au-rGO) nanocomposite thin films with enhanced electro-active characteristics were prepared and covalently immobilized with uricase (UOx) enzyme for sensitive and selective detection of uric acid (UA). Differential pulse voltammetry (DPV) studies revealed rapid response of fabricated electrode towards UA at low potential (0.228 V) in a wide concentration range of 50–800 μM with a sensitivity of 86.62 ± 0.19 μA mM^{-1} and very low detection limit of 7.32 ± 0.21 μM. The obtained Michaelis-Menten constant (k_m) value of 51.75 μM signifies high enzyme kinetics at electrode surface with UA. The developed biosensor was successfully applied to detect UA in human serum samples. Interferences due to components present in the real matrix were evaluated and UA determination in mixed sample was also performed. The fabricated UOx/Au-rGO/ITO biosensor demonstrated high reproducibility and a shelf-life of 6 months indicating the promising future of Au-rGO nanocomposite as an efficient transducer matrix for biosensing applications. The fast response time (1.0 ± 0.6 s) and improved sensor performance is attributed to the synergistic electronic properties of Au-nanoparticles and rGO that provided enhanced electron transfer and high electro-active species surface coverage at Au-rGO nanocomposite.

1. Introduction

Development of innovative and rapid disease diagnosis techniques remains one of the major thrust areas of modern day biomedical research [1]. Identification, detection and quantification of metabolites that govern important biochemical processes in human body, carve out a niche for fast, easy and accurate diagnosis of various diseases. Uric acid (UA), is a common metabolite released in blood serum as a result of catabolism of purine and is removed from the body following the urinary excretion without undergoing further metabolism [2]. Its increased concentration in blood is associated with several medical conditions such as gout [3], Lesch-Nyhan syndrome [4], diabetes, renal dysfunction and cardiovascular diseases [5]. The concentration range of UA in healthy human blood is estimated to be 130–460 μM [6]. Monitoring of UA levels, therefore, becomes imperative for diagnosis and prescription of treatments for these diseases. Conventional clinical methods used for detection of UA are based on spectrophotometry [7], fluorimetry [8,9], high-performance liquid chromatography (HPLC) [10], capillary electrophoresis [11], liquid chromatography-mass spectrometry (LCMS) [12,13] etc. These techniques, despite being expedient bear shortcomings in terms of low specificity, requirement of high sample amount, skilled manpower, costly laboratory setup and inability for on-spot analysis.

Electrochemical biosensing has emerged as a fast, accurate, inexpensive and portable technique for determination of electro-active metabolites like UA at sub-micro levels [14,15]. The electro-oxidizable property of UA has been used for its direct quantitative/qualitative determination [16,17]. Uricase (urate oxidase, UOx), a copper-containing homotetrameric enzyme that catalyzes the oxidation reaction of UA to produce allantoin and hydrogen peroxide [18] has proven to be immensely fruitful for its selective detection [2,19].

$$\text{Uric acid} + H_2O + O_2 \xrightarrow{\text{Uricase}} \text{Allantoin} + H_2O_2 + CO_2$$

$$H_2O_2 \rightarrow 2H^+ + O_2 + 2e^-$$

The long-established method involves detection of enzymatically oxidized UA by monitoring the formation of hydrogen peroxide at the working electrode. However, the oxidation of H_2O_2 takes place at high potentials i.e. > 0.4 V, thus subjecting the sensor to the risk of signal

* Corresponding author at: Bhartiya Nirdeshak Dravya Division, CSIR - National Physical Laboratory, New Delhi 110012, India.
E-mail address: singhsp@nplindia.org (S.P. Singh).

https://doi.org/10.1016/j.ijbiomac.2019.02.121
0141-8130/

falsification due to interference from other biological metabolites such as ascorbic acid and various amino acids with similar oxidation potentials [2,20]. This drawback can be eliminated by using redox mediators (as substitute for oxygen) that scavenge the electrons from active sites of the enzyme thus facilitating oxidation of UA at lower potentials [14,21]. This biochemical reaction could efficiently be monitored by designing a suitable electrochemical biosensor. The identification of biochemical events at electrode surface in a biosensor require a suitable transducer matrix that could enable fast charge transfer, facile immobilization of enzyme and provide homeostatic microenvironment for enzyme activity and stability. Biosensors based on different transducer matrices such as engineered carbon materials [22], metal or metal oxide nanoparticles [23], conducting polymers [24] have been proposed, which demonstrate reasonably good sensitivity towards UA, nevertheless, the low enzyme activity, sluggish electrode kinetics, interference due to high overpotentials and cumbersome fabrication process still present some of the major drawbacks [2]. Therefore, it is of great importance to develop a highly efficient matrix in view of achieving greater precision for detecting UA at very low concentrations at faster rate without any interference.

Herein, we report an enzymatic electrochemical biosensor based on gold nanoparticles-reduced graphene oxide (Au-rGO) nanocomposite thin films for sensitive and selective detection of UA. The Au-rGO nanocomposite offers the effective covalent immobilization of uricase enzyme through amide linkage to its surface due to the presence of carboxylic groups of rGO. The integration of Au-nanoparticles (AuNPs) to two-dimensional rGO sheets imparts good conductivity and high electron transfer rate, required to fabricate sensor with enhanced response towards UA.

2. Methodology

2.1. Reagents and techniques

Uricase (source: *Candida* sp.) ≥ 2 U/mg lyophilized powder, gold(III) chloride hydrate ($HAuCl_4$), potassium hexacyanoferrate(III) ($K_3Fe(CN)_6$), potassium hexacyanoferrate(II) trihydrate ($K_4Fe(CN)_6 \cdot 3H_2O$), N-hydroxysuccinimide (NHS), N-ethyl-N′-(3-dimethylaminopropyl) carbodiimide hydrochloride (EDC), potassium phosphate monobasic (KH_2PO_4), sodium phosphate dibasic dehydrate ($Na_2HPO_4 \cdot 2H_2O$), ethanolamine ($HOCH_2CH_2NH_2$) and sulphuric acid (H_2SO_4) were purchased from Sigma-Aldrich. Solvents i.e. acetone and isopropyl alcohol were purchased from Alfa Aesar. Potassium permanganate ($KMnO_4$), trisodium citrate ($Na_3C_6H_5O_7$), sodium nitrate ($NaNO_3$), sodium chloride (NaCl), potassium chloride (KCl) and hydrogen peroxide (H_2O_2) were procured from Merck. Graphite powder was obtained from Acros Organics. ITO glass substrates with glass thickness of 1 mm and resistivity of 15–20 Ω cm were bought from Macwin India. Serum samples for analysis were collected from Rao Tularam Memorial Hospital, Delhi, India.

Powder x-ray diffraction patterns of the synthesized nanomaterials were recorded on Rigaku miniflex-300 bench top X-Ray diffractometer having Cu Kα (λ = 1.541 Å) X-ray source. Agilent-Cary-NIR 5000 was used to measure the optical features of the samples in the range 200–800 nm. The infrared spectra were measured in ATR mode using Agilant Cary 360 FTIR spectrometer. Raman measurements were conducted on Ranishaw win-via reflex spectrometer within the spectral range of 200–2000 cm^{-1}. The atomic scale images were collected using Technai G2 F30 STWIN field emission transmission electron microscope source at electron accelerating voltage of 300 kV. Atomic Force Microscope nanoscope (Veeco V) was used to capture topographical image of the thin films in tapping mode. Cyclic voltammetry (CV) and differential pulse voltammetry (DPV) measurements were carried out in 3 mM Zobell's solution (containing 1 *m* KCl with equimolal amounts of $K_4Fe(CN)_6 \cdot 3H_2O$ and $K_3Fe(CN)_6$) using PalmSens3 potentiostat equipped with a three-electrode cell setup where Pt wire mesh, Ag/AgCl and the prepared Au-rGO thin films were used as counter, reference and working electrodes, respectively.

2.2. Synthesis of Au-rGO nanocomposite

Modified Hummer's method was used for synthesis of graphene oxide (GO) [25]. Au-rGO nanocomposite was synthesized using previously reported procedure published elsewhere [26]. Briefly, 0.5 mL of 25 mM $HAuCl_4.3H_2O$ solution was mixed with 25 mL homogeneous solution of pre-synthesized GO (0.1 mg/mL) in water at constant stirring for 30 min. The temperature of the solution was then raised to 90 °C and 2.5 mL of solution containing 0.0323 g of trisodium citrate dihydrate was added to it once the reaction reached to boiling condition. This solution was stirred for 30 min at 90 °C to accomplish the citrate based reduction process which was marked by appearance of reddish-brown colour. Afterwards, it was cooled to room temperature, and centrifuged at 7000 rpm for 15 min to remove unbound materials. Finally, the obtained pellet was lyophilized to get a fluffy reddish-brown powder of the Au-rGO nanocomposite.

2.3. Fabrication of UOx/Au-rGO/ITO biosensor

For the fabrication of biosensor, indium-tin oxide (ITO) coated glass (5×6 mm^2) was used as substrate. Before use, ITO coated glass substrates were thoroughly cleaned by sonication in detergent, acetone, isopropanol and deionized water. Thin films of Au-rGO nanocomposite were then prepared by applying two coats of aqueous solution of Au-rGO (0.5 mg/mL) on the cleaned ITO-substrates using spin coating technique. Here, 40 μL of Au-rGO solution was dispensed onto the ITO-substrate and rotated at 3000 rpm (with acceleration of 500) for 1 min. After spin coating, these films were annealed at 100 °C for 3 h. Then, 50 μL of homogeneous mixture of 0.5 M EDC and 0.1 M NHS (1:1 *v*/v) was dropcasted onto the surface of prepared thin films and incubated for 40 min at room temperature in order to activate the carboxylic groups of GO. The unreacted EDC-NHS was removed by washing the films with deionized water. In the next step, 20 μL of uricase enzyme (1 unit/mL in 50 mM phosphate buffer saline of pH -7) was immobilized on the activated surface of each of the films and was incubated for 5 h to achieve binding of uricase with thin film surface through covalent amide linkage. The films were finally drop-casted with 0.1 M ethanolamine to block the unbound active sites. Fig. 1 shows the schematic for the fabrication of biosensor.

3. Results and discussions

3.1. Characterization of Au-rGO nanocomposite

The synthesized Au-rGO nanocomposite was thoroughly examined using different characterization tools to understand its structural and morphological properties. Powder x-ray diffraction pattern of Au-rGO nanocomposite (Fig. 2a) displays the diffraction from the (002) plane appearing as a broad hump at 2θ value ~23° [26,27] pertaining to formation of rGO skeleton, and sharp diffraction peaks at 2θ values of 38.12, 44.29 and 64.57° matching to the (111), (200) and (220) planes of fcc structure of gold (JCPDS no. 04-0784) [26,28]. UV–visible spectroscopy studies further confirmed the formation of AuNPs on rGO surface (Fig. 2b). The spectrum of Au-rGO retains the peaks for π-π* (at 232 nm) and n-π* (at 304 nm) transitions from its parent compound GO [29], with feeble intensities, indicating loss of some of the functionalities and intercalated water molecules from the structure. The prominent absorption peak observed at 524 nm is due to the surface plasmon resonance (SPR) which is a phenomenon arising from the collective oscillation of the free electrons present at the surface of AuNPs on interaction with incident photons [30]. Fig. 2c shows the TEM images of Au-rGO where spherical AuNPs of 16–18 nm size could be seen scattered

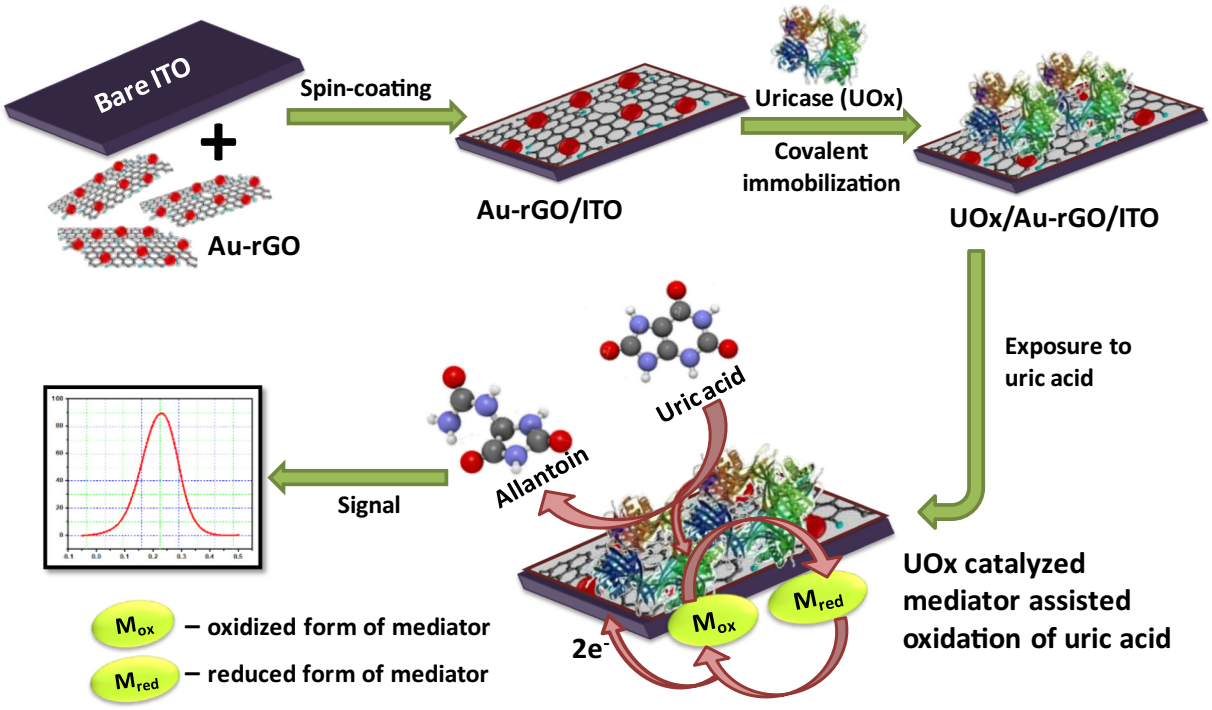

Fig. 1. Schematic showing biosensor fabrication process and UA detection.

uniformly across the wrinkled rGO sheets clearly visible in the marked rectangular regions. Further, the HR-TEM image revealed formation of highly crystalline AuNPs with the interplaner spacing of 2.34 Å matching well with the literature [31].

3.2. Electrochemical studies of prepared thin films

The reversible/irreversible electrochemical behaviour of spin coated Au-rGO/ITO thin films was investigated comprehensively by subjecting

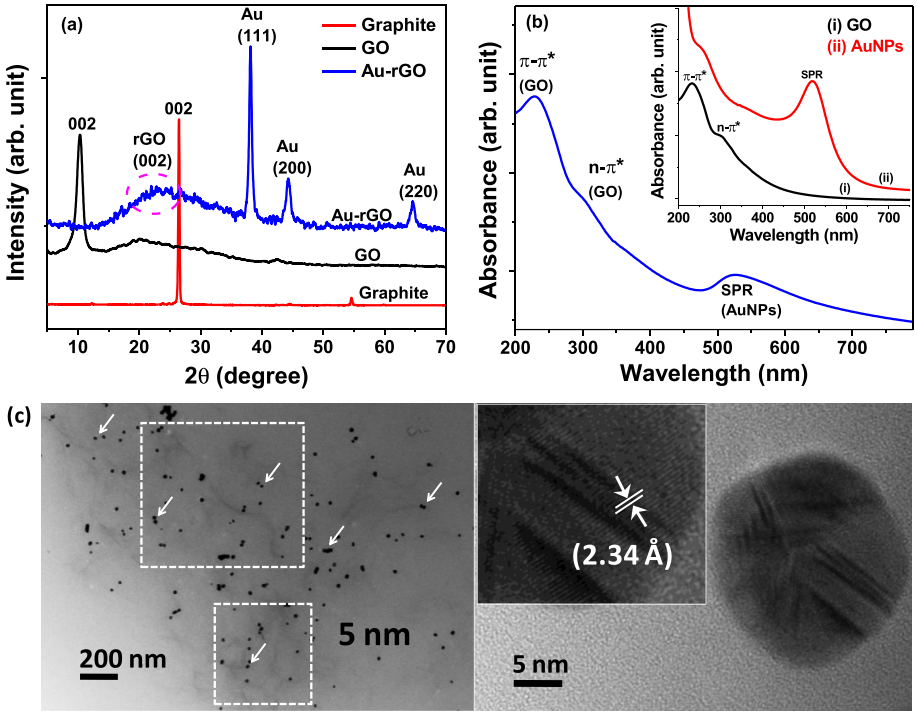

Fig. 2. (a) Powder x-ray diffraction patterns of graphite, GO and Au-rGO. (b) UV–visible spectrum of aqueous solution of Au-rGO. [Inset figure shows UV–visible spectra of GO and AuNPs for comparison]. (c) TEM micrographs of Au-rGO nanocomposite deposited on carbon-coated copper grid with 200-mesh at 200 nm scale showing distribution of AuNPs (indicated by arrows) across the rGO sheet (highlighted by the rectangular portion) and at 5 nm scale showing morphology of the AuNPs with inset showing the interplaner spacing in the selected grain.

the films to CV measurements in 3 mM Zobell's solution at different scan rates ranging from 0.01 to 0.12 Vs^{-1} (Fig. 3a). The redox activity of ferro-ferri couple got enhanced with increasing scan rate value which was evident from the subsequent increase in redox peak currents (I_p). The Au-rGO/ITO electrode showed positive shift of potential in anodic peak current (I_{pa}) and negative shift of potential in cathodic peak current (I_{pc}) with increasing scan rate causing ΔE_p ($= E_{pa}–E_{pc}$) to increase, thus indicating towards quasi-reversible kinetics [32]. The I_{pa} and I_{pc} values were plotted against the square root of scan rate ($\nu^{1/2}$) as shown in the inset of Fig. 3a. The plot with straight line fitting showed linear dependence of peak current magnitudes on square roots of scan rates (regression coefficient value, R^2 of 0.99733 for I_{pa} and 0.99537 for I_{pc}) thus marking the occurrence of diffusion controlled redox process at the electrode-electrolyte interface [32,33]. The relationship between I_p and $\nu^{1/2}$ was further described by Randles-Sevcik equation [32,33] given below (Eq. (1)).

$$I_p = \left(2.69 \times 10^5\right) n^{3/2} A\, C\, D^{1/2}\, \nu^{1/2} \quad (1)$$

where I_p is the anodic/cathodic peak current (in amperes), n is the number of transferred electrons at the electrode interface, A is the surface area of electrode (in cm^2), C is the concentration of the redox species (in mol cm^{-3}), D is the diffusion coefficient ($cm^2\ s^{-1}$) and ν is the scan rate (in $V\ s^{-1}$). Using Eq. (1), the diffusion coefficient associated with the ongoing redox process at Au-rGO/ITO electrode was determined to be $1.2053 \times 10^{-5}\ cm^2\ s^{-1}$. All these results are in good agreement with our previous results for same matrix [26].

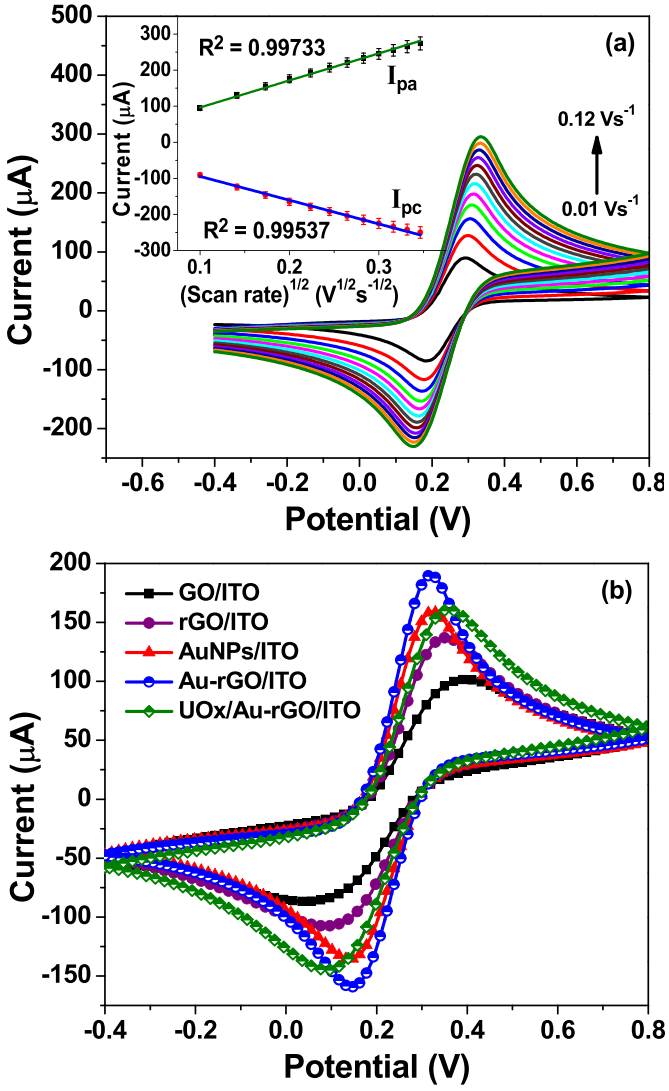

Fig. 3. (a) Cyclic voltammetry curves recorded at Au-rGO electrode in 3 mM Zobell's solution as a function of scan rates. [Inset shows the plot of anodic/cathodic current with square root of scan rate.] (b) Cyclic voltammetry curves for electrodes at each surface modification step recorded at scan rate of 0.05 Vs^{-1} in 3 mM Zobell's solution.

Further, the electrochemical activities of differently modified electrodes (i.e. GO/ITO, rGO/ITO, AuNPs/ITO, Au-rGO/ITO and UOx/Au-rGO/ITO) were determined by carrying out a comparative analysis of CV curves obtained at a fixed scan rate (0.05 Vs^{-1}) for redox reaction of $[Fe(CN)_6]^{3-/4-}$ mediator at each electrode modification step (Fig. 3b). The parameters like redox current (I_{pa} and I_{pc}), ΔE_p and FWHM of redox peaks for each case has been tabulated in Table 1. From Fig. 3b it can be seen that slow electron transfer kinetics was observed for GO/ITO electrode which is characterized by the low redox current values along with high ΔE_p and peak broadness in comparison to all other electrodes. The electron transport improves as we go from GO/ITO to rGO/ITO electrode causing increase in redox current and decrease in ΔE_p because of high C/O ratio after partial restoration of π-network in carbon structure that channelizes the electron flow [34]. A further enhancement in redox current values with fall in ΔE_p value is seen for AuNPs/ITO electrode owing to its inherent property of acting as conduction pockets to promote electron transfer [35]. The voltammogarm obtained at Au-rGO/ITO electrode showed highest redox current values and low ΔE_p value signifying superior electron transfer property of the synthesized nanocomposite. This is attributed to the combined effect of conductive AuNPs attached on rGO matrix that facilitate wiring of electrons from electrolyte to electrode surface [26,36] and the efficient charge transfer process in rGO due to presence of delocalized π-electrons across the sp^2 carbon network. However, the immobilization of enzyme molecules on Au-rGO/ITO films led to a drop in redox current of ferro-ferri couple at UOx/Au-rGO/ITO electrodes in comparison to Au-rGO/ITO electrode. The observed slower redox kinetics at the enzymatic electrode is attributed to the non-conducting nature of the macromolecule that hinders the electron transfer process.

3.3. Characterization of uricase-immobilized electrode (UOx/Au-rGO/ITO)

The immobilization of uricase on Au-rGO/ITO films was established using FTIR and AFM measurements. A comparison of FTIR spectra of Au-rGO and UOx/Au-rGO films is shown in Fig. 4a. The sharp band at 3280 cm^{-1} in the FTIR spectrum of UOx/Au-rGO film belongs to the stretching frequency of amide N—H group. The bands in the range of 2962–2850 cm^{-1} correspond to C—H stretches of alkyl and alkenyl groups. C═O stretches of primary and secondary amides in the uricase enzyme appear at 1630 and 1550 cm^{-1} respectively, while a sharp band for C—N stretch of amine group is observed at 1245 cm^{-1}. Other peaks corresponding to hydroxyl O—H bend, carboxyl C—O and alkoxy C—O stretches are observed at 1452, 1366, 1053 cm^{-1} respectively. Presence of stretching frequencies relating to amide groups confirms the immobilization of uricase on the film surface. Further, AFM micrographs of Au-rGO/ITO and UOx/Au-rGO/ITO at 3.0 μM scale are also given in Fig. 4b. The image of Au-rGO/ITO exhibited nanostructured surface morphology of the grains with roughness of 0.74 nm. On the other hand, the image of UOx/Au-rGO/ITO electrode exhibited modified surface topography with increased average roughness of 3.19 nm indicating the successful immobilization of enzyme on the Au-rGO electrode surface.

3.4. Detection of UA using UOx/Au-rGO/ITO bioelectrode

The analytical response measurements of the fabricated enzymatic biosensor was performed using a more sensitive technique i.e. DPV operated at pulse potential of 0.02 V with pulse time 0.07 s at the scan rate of 0.02 Vs^{-1}. The optimization of pH conditions for better performance of biosensor was done by exposing the sensor to a fixed concentration of UA (i.e. 200 μM) at different pH conditions (inset of Fig. 5a). An increase

Table 1
Comparison of peak parameters of cyclic voltammograms obtained for redox reaction of $[Fe(CN)_6]^{3-/4-}$ mediator at different electrode modifications ($n = 3$, RSD < 4.2%).

Electrode	Anodic signal		Cathodic signal		ΔE_p (V)
	I_{pa} (μA)	FWHM (V) (anodic peak)	I_{pc} (μA)	FWHM (V) (cathodic peak)	
GO/ITO	101.87 ± 4.16	0.31	- (86.14 ± 3.51)	0.39	0.34
rGO/ITO	137.03 ± 5.51	0.25	- (107.45 ± 4.58)	0.36	0.26
AuNPs/ITO	159.31 ± 4.58	0.21	- (136.22 ± 4.51)	0.25	0.18
Au-rGO/ITO	190.01 ± 3.05	0.19	- (160.13 ± 4.73)	0.24	0.17
UOx/Au-rGO/ITO	161.29 ± 4.04	0.26	- (144.81 ± 2.64)	0.32	0.27

in peak current is observed at pH ranging from 5.5 to 7.0. However, the increase in current stops at pH 7.0 and starts decreasing thereafter (i.e. till 8.0). Therefore, pH 7.0 was chosen as the optimum pH condition at which the sensor showed optimum response towards UA.

Fig. 5a shows the DPV response curves of UOx/Au-rGO/ITO biosensor towards UA over a concentration range of 50–1000 μM. The biosensor exhibited sharp and stable oxidation peaks that may be attributed to fast electron transfer over the entire concentration profile. A subsequent increase in the current values was observed with increasing UA concentration at the bioelectrode in presence of mediator $[Fe(CN)_6]^{3-/4-}$ that facilitated catalytic oxidation of UA. The redox mediator shuttles the electrons from enzyme to the electrode surface causing direct electron transfer between the two instead of the analyte and electrode, thus allowing the detection of analyte at low potentials [33,37]. The mechanism for detection of uric acid via redox mediator $[Fe(CN)_6]^{3-/4-}$ is illustrated by the following reactions (Eqs. (2)–(4)) occurring at the electrode surface.

$$\text{Uric acid} + 2H_2O + \text{Uricase(ox)} \rightarrow \text{Allantoin} + CO_2 + 2H^+ + \text{Uricase(red)} \quad (2)$$

$$\text{Uricase(red)} + 2\left[Fe(CN)_6\right]^{3-} \rightleftharpoons \text{Uricase(ox)} + 2\left[Fe(CN)_6\right]^{4-} \quad (3)$$

$$2\left[Fe(CN)_6\right]^{4-} \rightleftharpoons 2\left[Fe(CN)_6\right]^{3-} + 2e^- \quad (4)$$

Uricase catalyzes the oxidation of UA into water soluble allantoin and thereby it gets reduced. The ferricyanide ions present in the electrochemical cell, extract the electrons from the redox centres of reduced enzyme molecules causing conversion of enzyme back to its active form. In this process, the ferricyanide ions get reduced to ferrocyanide ions, therefore, increasing the concentration of ferrocyanide ions in the vicinity of the electrode surface suggesting that concentration of uric acid being oxidized is directly proportional to the increase in concentration of ferrocyanide ions. The ferrocyanide ions get oxidized under the applied potential, releasing electrons at the electrode surface and result into enhancement in peak current. The schematic depicting the reaction mechanism at electrode-electrolyte interface is shown in Fig. 5b.

The dependence of current on UA concentration in the range 50–800 μM was found to be linear as evident from the calibration plot (Fig. 5c) having the linear regression equation as: $\Delta I = 0.0866\,[UA] + 19.3695$ with the correlation coefficient value of 0.9955. The sensitivity of the biosensor as calculated from the calibration plot of current vs. concentration was found to be 86.62 ± 0.19 μA mM^{-1} ($n = 3$). The value for limit of detection (LOD) was obtained using the Eq. (5) [38,39].

$$LOD = k \times (\sigma/S) \quad (5)$$

Here, k is the confidence level parameter, σ is the standard deviation of control measurements, and S is the sensitivity. The LOD of 7.32 ± 0.21 μM ($n = 3$ at 95% confidence level) exhibited by the biosensor is appreciably lower than the clinically significant ranges of UA concentration in human serum. The remarkable sensitivity and a detection limit well below the physiological range, achieved by the biosensor may be attributed to the expected synergistic role of Au decorated rGO nanosheets that enables proficient signal transduction and effective electrocatalytic activity. The response time of the UOx/Au-rGO/ITO biosensor towards UA was determined using chronoamperometry as shown in inset of Fig. 5c. The obtained result shows increment in current response within 1.0 ± 0.6 s of each subsequent addition of UA thus revealing the ability of the sensor for ultrafast detection of UA.

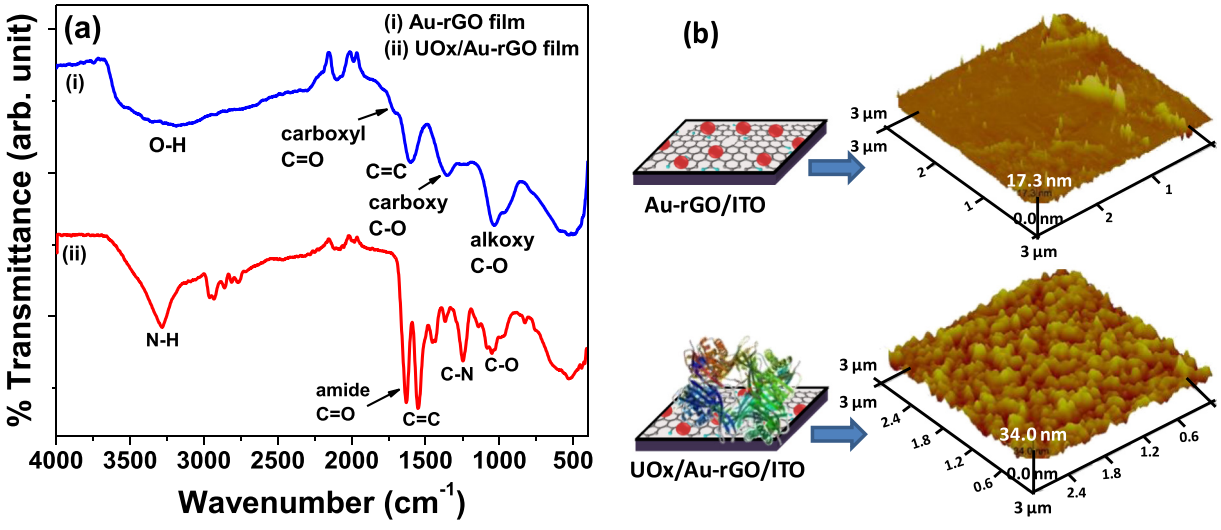

Fig. 4. (a) FTIR spectra and (b) 3-D AFM images of Au-rGO/ITO and UOx/Au-rGO/ITO.

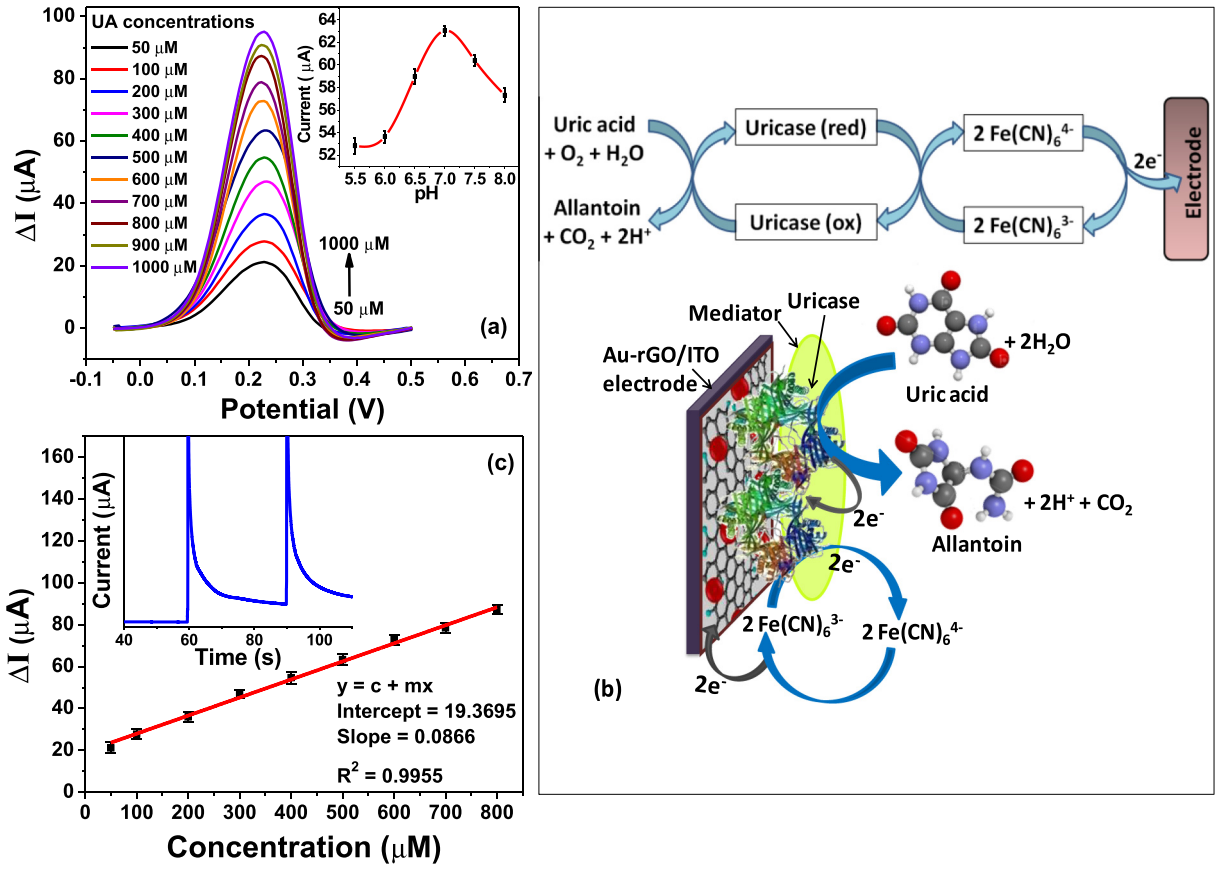

Fig. 5. (a) DPV curves showing response of UOx/Au-rGO/ITO biosensor towards UA in the concentration range of 50–1000 μM. [Inset shows effect of working buffer pH on the sensor response] (b) Schematic showing the mechanism of mediator-assisted electron transfer process taking place at the electrode-electrolyte interface due to enzyme catalyzed oxidation of UA. (c) Calibration plot between the changes in current signal with respect to the exposed concentration of UA. [Inset shows the chronoamperometry curve for detection of UA using UOx/Au-rGO/ITO biosensor].

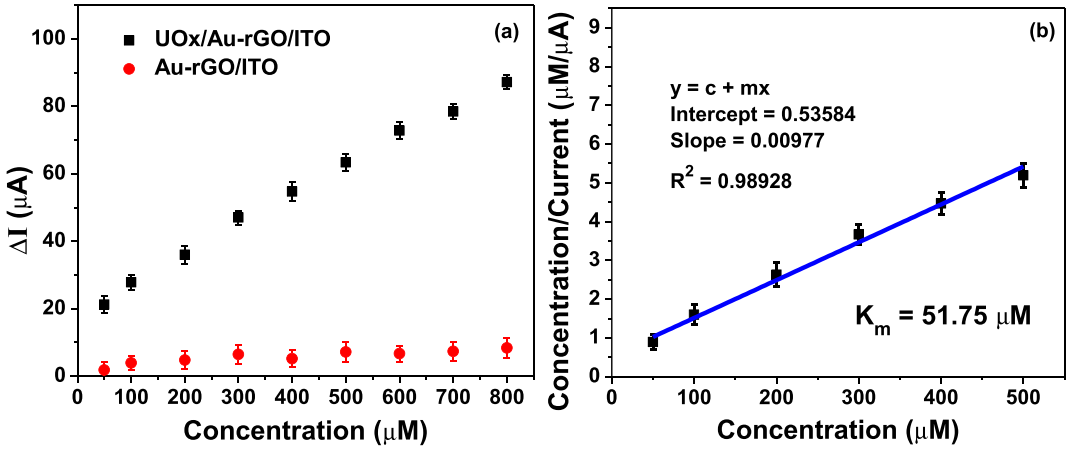

Fig. 6. (a) Plot showing change in current values obtained with respect to different concentrations of UA using enzyme-based and enzyme-free Au-rGO/ITO electrode (i.e. control set). (b) Hanes plot for determination of k_m value of the immobilized enzyme.

To validate the significant role-play of enzyme kinetics in UA determination, a negative control was performed by detecting different concentrations of UA using enzyme-free electrode i.e. Au-rGO/ITO (Fig. 6a). It was noteworthy to observe diminutive and irregular change in current values in comparison to that obtained using uricase enzyme-based bioelectrodes. Therefore, it gave a straightforward visualization of catalytic effect of uricase enzyme in oxidation of UA causing a substantial measurable change in oxidation peak current consequently leading to effortless quantification of UA. Hanes plot was constructed

Table 2
Determination of UA concentrations in spiked serum samples.

Spiked UA concentration C_s (μM)	Recovered UA concentration C_i - C_o (μM)	% Recovery	Relative standard deviation(RSD) % ($n = 3$)
50	45.71	91.42	2.66
100	94.03	94.03	2.13
200	190.36	95.18	1.89
300	265.30	88.43	2.34
400	388.52	97.13	2.07

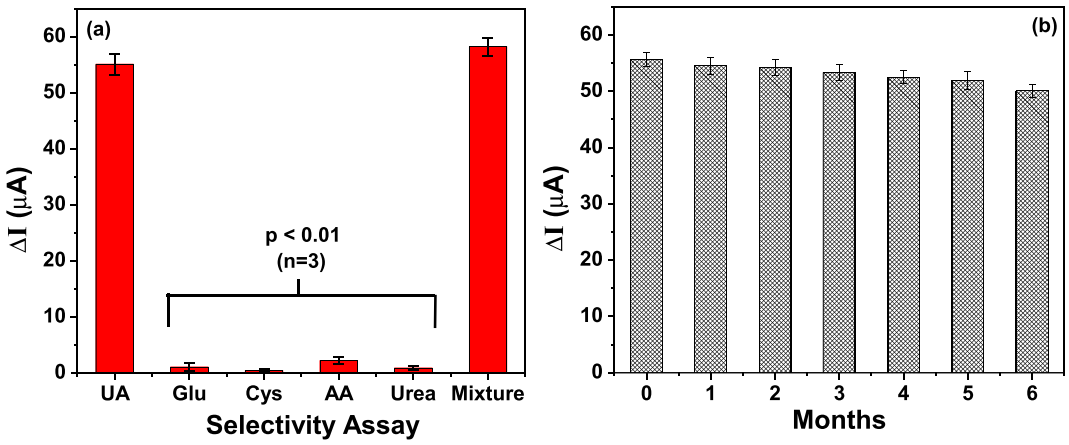

Fig. 7. Bar graphs showing (a) response of UOx/Au-rGO/ITO biosensor towards non-target analytes individually and towards UA in mixed sample of non-specific analytes, (b) response of the biosensor over a period of 6 months to evaluate its stability.

between [UA conc.]/current and [UA conc.] to determine the Michaelis-Menten constant (k_m) value for the immobilized uricase enzyme as shown in Fig. 6b. A very low magnitude of k_m i.e. 51.75 μM was calculated from the plot which signifies high binding affinity of the enzyme for UA.

The application of UOx/Au-rGO/ITO biosensor for real samples was demonstrated by detecting UA in spiked human serum sample. The UA concentration in the serum sample was determined using standard addition method. The serum sample was spiked with known concentrations (50, 100, 200, 300 and 400 μM) of UA and their levels were calculated by comparing the response current with the standard calibration curve. The % recovery value for each spiked concentration was calculated using Eq. (6) [26].

$$\%Recovery = \frac{C_i - C_o}{C_s} \times 100 \quad (6)$$

where C_i is the total concentration of analyte in the spiked samples estimated from the calibration plot, C_o is the concentration of analyte in unspiked sample and C_s is concentration of analyte spiked into the sample. The % recovery values for the spiked samples (given in Table 2) ranged from 88 to 98% suggesting negligible matrix effect of the biological constituents on the fabricated sensor and further validated its efficiency towards UA detection in clinical settings.

3.5. Selectivity and stability studies

Fig. 7a demonstrates the selectivity of the biosensor determined by investigating its performance in presence of non-target analytes. Commonly found interferents in body fluids such as glucose (Glu), L-cystein (Cys), ascorbic acid (AA) and urea were chosen for detection by the fabricated biosensor. The measurement was done for samples made in Zobell's solution containing UA and each of the interferent in 1:1 ratio. A mixture of all the interferents with UA was also analysed. The selectivity coefficient (k_{sel}), for the biosensor was determined using the Eq. (7) [33,40] and is given in Table 3.

$$k_{sel} = (Signal)_{interferent}/(Signal)_{UA} \quad (7)$$

The k_{sel} values in case of each interferent were found to be extremely low (i.e. $\ll 1$) which ascertained the specificity of the fabricated biosensor with the negligible response towards all the aforesaid interferents in comparison to UA. The non-interaction of immobilized uricase enzyme with these interferents was further established by conducting *t*-test [39] for the obtained data ($n = 3$) which gave t-value well within the acceptance region in all cases. Therefore, it can be concluded that the fabricated UOx/Au-rGO/ITO biosensor is competent in specifically detecting UA in real samples as well.

The reproducibility of the biosensor was examined by subjecting it to repeated measurements of 400 μM UA. The sensor showed almost similar response towards UA up to 42 successive cycles with RSD of 4.6% thus confirming its high reproducibility. The stability of the bioelectrode was monitored at stipulated intervals of time again by evaluating its response for 400 μM UA concentration. The bioelectrode was stored at 4 °C when not in use. The response of the biosensor after the time span of every month is depicted in Fig. 7b. The biosensor retained 98.0% activity at the end of 1 month which reduced to 97.4% after 2 months, then 95.9% after 3 months and dropped almost upto 90.0% at the end of 6 months. The acquired shelf-life data clearly testify the efficient utility of the fabricated biosensor for six months.

The following table (Table 4) shows the performance of the prepared biosensor in comparison to earlier reported sensors.

4. Conclusion

In summary, a robust matrix system i.e. Au-rGO based thin films having excellent electrochemical and biocompatible properties have been fabricated for sensitive, selective and low-cost detection of UA. The matrix allows facile immobilization of uricase on its surface through covalent attachment and facilitates longer shelf-life by retaining its bioactivity. The AuNPs decorated on atomically thin two-dimensional rGO sheets enabled efficient electron wiring property at the electrode interface causing rapid electron mobility. Consequently, the UOx/Au-rGO/ITO biosensor could successfully detect UA at wide concentration range of 50–800 μM with fairly low detection limit of 7.32 ± 0.21 μM (almost 20 times below the normal range of UA in serum). In addition,

Table 3
Determination of effect of interferents on biosensor performance using selectivity coefficient calculation and *t*-test.

Metabolite	Current (μA)	Interferent	Current (μA)	Selectivity coefficient calculation, k_{sel}	(Paired t-test) Interference
UA	55.055				
UA + Glu	56.128	Glu	1.073	0.019	No
UA + Cys	55.495	Cys	0.440	0.008	No
UA + AA	57.257	AA	2.202	0.040	No
UA + Urea	55.928	Urea	0.873	0.016	No
Mixture	58.202	Mixture (excl. UA)	3.147	0.057	No

Table 4
Comparison of enzymatic UA biosensors with the present study.

S. No.	Matrix	Immobilization method	Potential	Detection range	Sensitivity	Limit of detection	Time	K_m	Technique	Reference
1.	Uricase/NiO/Pt/Ti/glass	Physical	0.4 V	0.05–1 mM	1278.48 μM mM^{-1}	0.11 mM	5 s	0.17 mM	Cyclic voltammetry	[41]
2.	Uricase/AuNPs/MWCNTs/Au	Covalent	1.1 V	0.01–0.8 mM	0.44 mA mM^{-1}	0.01 mM	7 s	0.5 mM	Cyclic voltammetry	[42]
3.	Uricase/CuO/Pt/glass	Physical	0.1 V	0.05–1 mM	2.7 mA mM^{-1}	0.14 mM	4 s	0.12 mM	Cyclic voltammetry	[23b]
4.	Nafion/Uricase/ZnO/Au	Physical	0.59 V	0.1–0.59 mM	89.74 μA cm^{-2} mM^{-1}	25.6 μM	–	0.99 mM	Amperometry	[43]
5.	Uricase/Prussian blue/SPE	Physical	–	0.03–0.3 mM	–	0.01 mM	2 min	–	Cyclic voltammetry	[44]
6.	Nafion/Uricase/Ferrocene/GCE	Physical	0.342	500 nM-600 μM	1.78 μA $μM^{-1}$	230 nM	5 s	14.07 μM	Amperometry	[45]
7.	L-Met-FcAld/Au/Cu	Chemical	0.32	0–2.38 mM	72.8 μAmM^{-1}	2.4 μM	5 s	–	Cyclic voltammetry	[40]
8.	Uricase/Au-rGO/ITO	Chemical	0.228	50–800 μM	86.62 ± 0.19 μA mM^{-1}	7.32 ± 0.21 μM	1.0 ± 0.6 s	51.75 μM	Differential pulse voltammetry	Our study

it exhibited excellent reusability and high specificity towards UA in presence of non-target analytes. Furthermore, the low-cost and hassle-free fabrication process makes it a potential analytical platform for development of *point-of-care* systems for detection of UA and similar metabolites.

Acknowledgements

The authors thank the Director, NPL for providing with research facilities. SV gratefully acknowledges CSIR (31/01/(0510)/2018-EMR-1) India for financial assistance and SPS sincerely acknowledges the support from Network project BSC0112.

References

[1] (a) P. Chandra, Nanobiosensors for Personalized and Onsite Biomedical Diagnosis, the Institution of Engineering and Technology, Michael Faraday House, United Kingdom, London, 2016;
(b) P. Chandra, T.Y. Nee, S.P. Singh, Next Generation Point-of-Care Biomedical Sensors Technologies for Cancer Diagnosis, Springer, Singapore, 2017.
[2] P.E. Erden, E. Kılıc, A review of enzymatic uric acid biosensors based on amperometric detection, Talanta 107 (2013) 312–323.
[3] K.L. Rock, H. Kataoka, J.-J. Lai, Uric acid as a danger signal in gout and its comorbidities, Nat. Rev. Rheumatol. 9 (2013) 13–23.
[4] W.L. Nyhan, The recognition of Lesch–Nyhan syndrome as an inborn error of purine metabolism, J. Inherit. Metab. Dis. 20 (1997) 171–178.
[5] M. Heinig, R.J. Johnson, Role of uric acid in hypertension, renal disease, and metabolic syndrome, Clev. Clin. J. Med. 73 (2006) 1059–1064.
[6] Y.-C. Luo, J.-S. Do, C.-C. Liu, An amperometric uric acid biosensor based on modified Ir–C electrode, Biosens. Bioelectron. 22 (2006) 482–488.
[7] D.L. Rocha, F.R.P. Rocha, A flow-based procedure with solenoid micro-pumps for the spectrophotometric determination of uric acid in urine, Microchem. J. 94 (2010) 53–59.
[8] N.E. Azmi, N.I. Ramli, J. Abdullah, M.A.A. Hamid, H. Sidek, S.A. Rahman, N. Ariffin, N.A. Yusof, A simple and sensitive fluorescence based biosensor for the determination of uric acid using H_2O_2-sensitive quantum dots/dual enzymes, Biosens. Bioelectron. 67 (2015) 129–133.
[9] J. Galbán, Y. Andreu, M.J. Almenara, S. de Marcos, J.R. Castillo, Direct determination of uric acid in serum by a fluorometric-enzymatic method based on uricase, Talanta 54 (2001) 847–854.
[10] D. Swinson, J. Snaith, J. Buckberryc, M. Brickley, High performance liquid chromatography (HPLC) inthe investigation of gout in palaeopathology, Int. J. Osteoarchaeol. 20 (2010) 135–143.
[11] W. Pormsila, S. Krähenbühl, P.C. Hauser, Capillary electrophoresis with contactless conductivity detection for uric acid determination in biological fluids, Anal. Chim. Acta 636 (2009) 224–228.
[12] X. Dai, X. Fang, C. Zhang, R. Xu, B. Xu, Determination of serum uric acid using high-performance liquid chromatography (HPLC)/isotope dilution mass spectrometry (ID-MS) as a candidate reference method, J. Chromatogr. B 857 (2007) 287–295.
[13] W. Kwon, J. Young, K.S. Suh, M. Kyoln, Simultaneous determination of creatinine and uric acid in urine by liquid chromatography–tandem mass spectrometry with polarity switching electrospray ionization, Forensic Sci. Int. 221 (2012) 57–64.
[14] N.J. Ronkainen, H.B. Halsallb, W.R. Heineman, Electrochemical biosensors, Chem. Soc. Rev. 39 (2010) 1747–1763, https://doi.org/10.1039/B714449K.
[15] K. Mahato, P.K. Maurya, P. Chandra, Fundamentals and commercial aspects of nanobiosensors in point-of-care clinical diagnostics, 3 Biotech. 8 (2018) 149.
[16] J. Du, R. Yue, Z. Yao, F. Jiang, Y. Du, P. Yang, Nonenzymatic uric acid electrochemical sensor based on graphene-modified carbon fiber electrode, Colloids Surf. A Physicochem. Eng. Asp. 419 (2013) 94–99.
[17] K.-C. Lin, T.-H. Tsai, S.-M. Chen, Performing enzyme-free H_2O_2 biosensor and simultaneous determination for AA, DA, and UA by MWCNT–PEDOT film, Biosens. Bioelectron. 26 (2010) 608–614.
[18] (a) F. Bonneté, D. Vivarès, Ch. Robert, N. Colloc'h, Interactions in solution and crystallization of Aspergillus flavusurate oxidase, J. Cryst. Growth 232 (2001) 330–339;
(b) N.C.M. Zanon, O.N. Oliveira Jr., L. Caseli, Immbolization of uricase enzyme in Langmuir and Langmuir-Blodgett films of fatty acids: possible use as a uric acid sensor, J. Colloid Interface Sci. 373 (2012) 69–74;
(c) G.D. Vogels, C.V.D. Drift, Degradation of purines and pyrimidines by microorganisms, Bacteriol. Rev. 40 (1976) 403–468.
[19] G. Rocchitta, A. Spanu, S. Babudieri, G. Latte, G. Madeddu, G. Galleri, S. Nuvoli, P. Bagella, M.I. Demartis, V. Fiore, R. Manetti, P.A. Serra, Enzyme biosensors for biomedical applications: strategies for safeguarding analytical performances in biological fluids, Sensors 16 (2016) 780.
[20] W. Putzbach, N.J. Ronkainen, Immobilization techniques in the fabrication of nanomaterial-based electrochemical biosensors: a review, Sensors 13 (2013) 4811–4840.
[21] C. Dhand, N. Dwivedi, S. Mishra, P.R. Solanki, V. Mayandi, R.W. Beuerman, S. Ramakrishna, R. Lakshminarayanan, B.D. Malhotra, Polyaniline-based biosensors, Nanobiosens. Dis. Diagn. 4 (2015) 25–46.
[22] (a) M.N. Omar, A.B. Salleh, H.N. Lim, A.A. Tajudin, Electrochemical detection of uric acid via uricase-immobilized graphene oxide, Anal. Biochem. 509 (2016) 135–141;
(b) H.-W. Yu, Z. Zhang, T. Shen, J.-H. Jiang, D. Chang, H.-Z. Pan, Sensitive determination of uric acid by using graphene quantum dots as a new substrate for immobilisation of uric oxidase, IET Nanotechnol. 12 (2018) 191–195.
[23] (a) F. Zhang, X. Wang, S. Ai, Z. Suna, Q. Wan, Z. Zhub, Y. Xian, L. Jin, K. Yamamoto, Immobilization of uricase on ZnO nanorods for a reagentless uric acid biosensor, Anal. Chim. Acta 519 (2004) 155–160;
(b) K. Jindal, M. Tomar, V. Gupta, CuO thin film based uric acid biosensor with enhanced response characteristics, Biosens. Bioelectron. 30 (2011) 333–336.
[24] H. Chu, X. Wei, M. Wu, J. Yan, Y. Tu, An electrochemiluminescent biosensor based on polypyrrole immobilized uricase for ultrasensitive uric acid detection, Sensors Actuators B Chem. 163 (2012) 247–252.
[25] L. Cote, F. Kim, J. Huang, Langmuir-Blodgett assembly of graphite oxide single layers, J. Am. Chem. Soc. 131 (2009) 1043–1049.
[26] S. Verma, A. Singh, A. Shukla, J. Kaswan, K. Arora, J. Ramirez-Vick, P. Singh, S.P. Singh, Anti-IL8/AuNPs-rGO/ITO as an immunosensing platform for non invasive electrochemical detection of oral cancer, ACS Appl. Mater. Interfaces 9 (2017) 27462–27474.
[27] I.K. Moon, J. Lee, R.S. Ruoff, H. Lee, Reduced graphene oxide by chemical graphitization, Nat. Commun. 1 (2010) 73.
[28] N. Zhang, H. Qiu, Y. Liu, W. Wang, Y. Li, X. Wang, J. Gao, Fabrication of gold nanoparticle/graphene oxide nanocomposites and their excellent catalytic performance, J. Mater. Chem. 21 (2011) 11080–11083.
[29] J. Zhang, H. Yang, G. Shen, P. Cheng, J. Zhang, S. Guo, Reduction of graphene oxide via L-ascorbic acid, Chem. Commun. 46 (2010) 1112–1114.
[30] (a) M.-K. Chuang, S.-W. Lin, F.-C. Chen, C.-W. Chub, C.-S. Hsu, Gold nanoparticle-decorated graphene oxides for plasmonic-enhanced polymer photovoltaic devices, Nanoscale 6 (2014) 1573–1579;
(b) Y.-C. Yeh, B. Creran, V.M. Rotello, Gold nanoparticles: preparation, properties, and applications in bionanotechnology, Nanoscale 4 (2012) 1871–1880.
[31] R. Torres-Mendieta, D. Ventura-Espinosa, S. Sabater, J. Lancis, G. Mínguez-Vega1, J.A. Mata, In situ decoration of graphene sheets with gold nanoparticles synthesis by pulsed laser ablation in liquids, Sci. Rep. 6 (2016), 30478. .
[32] A.J. Bard, L.R. Faulkner, Electrochemical Methods Fundamentals and Applications, John Wiley & Sons, Inc., 2001
[33] J. Wang, Analytical electrochemistry, John Wiley and Sons, Vol. 272 (2006).

[34] (a) A. Ambrosi, C.K. Chua, A. Bonanni, M. Pumera, Electrochemistry of graphene and related materials, Chem. Rev. 114 (2014) 7150–7188;
(b) A. Ambrosi, A. Bonanni, Z. Sofer, J.S. Cross, M. Pumera, Electrochemistry at chemically modified graphenes, Chem. Eur. J. 17 (2011) 10763–10770.
[35] J.M. Pingarron, P. Yanez-Sedeno, A. Gonzalez-Cortes, Gold nanoparticle-based electrochemical biosensors, Electrochim. Acta 53 (2008) 5848–5866.
[36] Y.-M. Yan, R. Tel-Vered, O. Yehezkeli, Z. Cheglakov, I. Willner, Biocatalytic growth of Au nanoparticles immobilized on glucose oxidase enhances the ferrocene-mediated bioelectrocatalytic oxidation of glucose, Adv. Mater. 20 (2008) 2365–2370.
[37] S. Kuwabata, T. Nakaminami, S. Ito, H. Yoneyama, Preparation and properties of amperometric uric acid sensors, Sensors Actuators B 52 (1998) 72–77.
[38] J.N. Tiwari, V. Vij, K.C. Kemp, K.S. Kim, Engineered carbon-nanomaterial-based electrochemical sensors for biomolecules, ACS Nano 10 (2016) 46–80.
[39] J. N. Miller, J. C. Miller, Statistics and Chemometrics for Analytical Chemistry, Sixth Ed., Pearson Education Limited, Essex, England, 2010.
[40] C. Cheng, C.-Y. Kao, An electrochemical biosensor with uricase immobilized on functionalized gold coated copper wire electrode for urinary uric acid assay, Electroanalysis 28 (2016) 695–703.
[41] K. Arora, M. Tomar, V. Gupta, Highly sensitive and selective uric acid biosensor based on RF sputtered NiO thin film, Biosens. Bioelectron. 30 (2011) 333–336.
[42] N. Chauhan, C.S. Pundir, An amperometric uric acid biosensor based on multiwalled carbon nanotube–gold nanoparticle nanocomposite, Anal. Biochem. 413 (2011) 97–103.
[43] Y. Zhao, X. Yan, Z. Kang, P. Lin, X. Fang, Y. Lei, S. Ma, Y. Zhang, Highly sensitive uric acid biosensor based on individual zinc oxide micro/nanowires, Microchim. Acta 180 (2013) 759–766.
[44] S. Piermarini, D. Migliorelli, G. Volpe, R. Massoud, A. Pierantozzi, C. Cortese, G. Palleschi, Uricase biosensor based on a screen-printed electrode modified with Prussian blue for detection of uric acid in human blood serum, Sensors Actuators B Chem. 179 (2013) 170–174.
[45] T. Ghosh, P. Sarkar, A.P.F. Turner, A novel third generation uric acid biosensor using uricase electro-activated with ferrocene on a Nafion coated glassy carbon electrode, Bioelectrochemistry 102 (2015) 1–9.